



Numerical investigation on flow process of liquid metals in melt delivery nozzle during gas atomization process for fine metal powder production

Chang LIU^{1,2}, Xin LI^{1,2}, Shi SHU³, Yu-he HUANG^{1,4}, Xing-gang LI^{1,2,4}, Qiang ZHU^{1,2}

1. Department of Mechanical and Energy Engineering,

Southern University of Science and Technology, Shenzhen 518055, China;

2. Shenzhen Key Laboratory for Additive Manufacturing of High-performance Materials, Shenzhen 518055, China;

3. Hunan Industrial Technical Center Co., Ltd., Changsha 410201, China;

4. Academy for Advanced Interdisciplinary Studies,

Southern University of Science and Technology, Shenzhen 518055, China

Received 22 September 2020; accepted 25 July 2021

Abstract: Based on volume of fluid (VoF) interface capturing method and shear-stress transport (SST) $k-\omega$ turbulence model, numerical simulation was performed to reveal the flow mechanism of metal melts in melt delivery nozzle (MDN) during gas atomization (GA) process. The experimental validation indicated that the numerical models could give a reasonable prediction on the melt flow process in the MDN. With the decrease of the MDN inner-diameter, the melt flow resistance increased for both molten aluminum and iron, especially achieving an order of 10^2 kPa in the case of the MDN inner-diameter ≤ 1 mm. Based on the conventional GA process, the positive pressure was imposed on the viscous aluminum alloy melt to overcome its flow resistance in the MDN, thus producing powders under different MDN inner-diameters. When the MDN inner-diameter was reduced from 4 to 2 mm, the yield of fine powder ($<150 \mu\text{m}$) soared from 54.7% to 94.2%. The surface quality of powders has also been improved when using a smaller inner-diameter MDN.

Key words: gas atomization; melt delivery nozzle; liquid metal; flow resistance; metal powder

1 Introduction

Metal additive manufacturing gains a promising expectation in the entire 3D printing system. Powder is the most commonly used feedstock form for metal 3D printing [1–3]. Compared with other conventional powder-based manufacturing techniques, metal 3D printing has higher requirements for metal powders in particle size, morphology, chemistry, etc. For example, the selective laser melting (SLM) process prefers metal powders which are in a size range of 15–45 μm , spherical or nearly spherical, and of low impurity [4]. Therefore, the production of metal

powders for additive manufacturing is supposed to be improved accordingly.

Currently, gas atomization (GA) is widely employed to produce metal powders for additive manufacturing [5], such as aluminum alloys [6–8], titanium alloys [9], iron alloys [10,11] and high-entropy alloys [12,13]. The main principle of this method is to use high speed gas to disintegrate molten metal into small droplets, which are finally solidified as metal powders [14]. The GA process is complicated due to the interaction between gas and liquid metals, which contains the breaking, cooling and solidification of the melt. Simultaneously, these sub-processes of the melt in turn affect the gas flow field. It is difficult to conduct direct experimental

investigation on the atomization process because the gas/melt interaction process is instantaneous under high temperatures. Therefore, numerical simulation is often employed as an aid to investigate intractable processes and help to understand the atomization process. TONG and BROWNE [15] adopted a unified model to describe the compressible gas flow without the melt. The density and pressure fields of the atomizing gas were well depicted. The difference of the discrete jet and annular slit gas nozzle was also revealed. MOTAMAN et al [16] combined numerical simulation and experiment to analyze the back-stream flow phenomenon which may lead to the lick-back of the melt. Besides, for the atomization process of the melt, ZEOLI et al [17] used the volume of fluid (VoF) method and the Reynolds stress model (RSM) to investigate the primary breakup of the melt. The gas flow field with the melt was compared to that without the melt. LI and FRITSCHING [18] adopted the VoF approach to describe the formation and disintegration process of the swirling conical sheets and the Eulerian–Lagrangian approach to describe the subsequent droplet spray process in the pressure–swirl–gas–atomization process. Meanwhile, some advanced optical detection techniques can be used to help to investigate the atomization process under lax conditions. LAMPA and FRITSCHING [19] adopted the particle image velocimetry (PIV) method to obtain the velocities of droplets and gas. MULLIS et al [20] used the high-speed imaging of the flow to examine the effect of melt delivery nozzle (MDN) geometry. SCHWENCK et al [21] obtained high speed images for different nozzle systems during cold gas atomization. It can be learned from the literature that, the gas flow field during the GA process has been investigated deeply and progress has also been made in studying the complicated multiphase flow processes of atomization and spray. However, little attention has been paid to the flow process of the melt in the MDN, although it is essential for the stability and continuity of the subsequent atomization process.

Normally, the molten metal is poured into the crucible and then flows out through the circular MDN installed at the bottom of the crucible. In order to control the melt discharge and obtain fine powders, the MDN inner-diameter is generally

controlled in the order of 10^0 – 10^1 mm. With the decrease of the MDN inner-diameter, the yield of fine powder usually increases greatly [22,23]. However, the metal melt which is, only driven by its own gravity and the aspiration pressure in front of the MDN exit, may not flow smoothly in the MDN with a very small inner-diameter, especially for those high viscosity alloys. In view of the limitation of the current detection methods, the melt flow process in the MDN cannot be directly observed. Thereby, the prediction of the melt flow resistance in the MDN was based on analytical or empirical formulas in our previous work [23]. In this work, numerical simulation tools were employed to quantify the melt flow resistance in the MDN. Based on the derived values of the melt flow resistance in the MDN, appropriate positive pressure (P_+) was imposed on the melt, ensuring that the melt could go through the MDN with a small inner-diameter. By this way, high viscosity aluminum alloy powders were prepared. The particle size and morphology were systematically analyzed.

2 Theory

2.1 Turbulence model

The shear-stress transport (SST) k - ω model was mainly tested in this work. Additionally, The Spalart–Allmaras (SA) model was introduced for comparison in flow resistance calculation. Both of the models above are Reynolds-averaged Navier-Stokes (RANS) models which are widely used in engineering due to their wide range of application and good balance between computational cost and accuracy. The Boussinesq hypothesis [24] is adopted in both models. Boussinesq hypothesis is written as Eq. (1), where the left part is Reynolds stress, ρ is the density, u is the velocity magnitude, k is the turbulence kinetic energy, and δ is the delta function. The core idea of such a model is to solve turbulent viscosity (μ_t). SA model [25] is a one-equation model, and only one additional transport equation (representing turbulent viscosity) is solved. μ_t is computed as Eqs. (2)–(4), where C_{v1} is a constant, ν is the kinematic viscosity, and $\tilde{\nu}$ is identical to ν except in the near-wall region. As for the SST k - ω model, it contains two types of models: k - ω model [26] and k - ε model [27]. Both are two-equation models. μ_t is a function of turbulence

kinetic energy (k) and specific dissipation rate (ω) or turbulence kinetic energy and turbulence dissipation rate (ε). In the SST k - ω model [28], μ_t is computed as Eqs. (5)–(7), where S is the strain rate magnitude, μ is the dynamic viscosity, y is the distance to the next surface, a is a constant, and α^* is the coefficient for low Reynolds number correction. This option was also introduced and designated as SST k - ω -LRe, and α^* is expressed as Eqs. (8)–(10).

$$-\rho \overline{u'_i u'_j} = \mu_t \left(\frac{\partial u_i}{\partial x_j} + \frac{\partial u_j}{\partial x_i} \right) - \frac{2}{3} \left(\rho k + \mu_t \frac{\partial u_k}{\partial x_k} \right) \delta_{ij} \quad (1)$$

$$\mu_t = \rho \tilde{\nu} f_{v1} \quad (2)$$

$$f_{v1} = \frac{\chi^3}{\chi^3 + C_{v1}} \quad (3)$$

$$\chi = \frac{\tilde{\nu}}{\nu} \quad (4)$$

$$\mu_t = \frac{\rho k}{\omega} \frac{1}{\max \left[\frac{1}{\alpha^*}, \frac{SF_2}{a\omega} \right]} \quad (5)$$

$$F_2 = \tanh \Phi^2 \quad (6)$$

$$\Phi = \max \left[2 \frac{k^{\frac{1}{2}}}{0.09\omega y}, \frac{500\mu}{\rho y^2 \omega} \right] \quad (7)$$

$$\alpha^* = \alpha_\infty^* \left(\frac{\alpha_0^* R_k + Re_t}{R_k + Re_t} \right) \quad (8)$$

$$Re_t = \frac{\rho k}{\mu \omega} \quad (9)$$

$$R_k = 6, \alpha_0^* = 0.024 \quad (10)$$

2.2 VoF model

VoF model is used to track the interface between the molten metal and the air. The volume fraction of the melt is defined as β_m . When $\beta_m=1$, the cell is full of the melt. When $\beta_m=0$, the cell is full of the air. If $0 < \beta_m < 1$, the cell contains the interface between the melt and the air. There is no mass transfer from the melt to the air and no new source term is defined, which are the hypotheses in the present case. Therefore, the transport equation of the volume fraction of the melt can be written as Eq. (11).

$$\frac{1}{\rho} \left[\frac{\partial}{\partial t} (\beta_m \rho) + \nabla \cdot (\beta_m \rho \vec{v}) \right] = 0 \quad (11)$$

where t is time, and v is overall velocity.

2.3 Flow resistance calculation

The flow of the melt through the MDN is mainly resisted by viscous shear stresses within the melt and the turbulence that occurs along the internal walls of the MDN. This melt flow resistance can be characterized by the pressure drop along the MDN. According to the Bernoulli equation [29] of the incompressible flow, the total pressure (P_0) is conserved on the same streamline. Therefore, the pressure drop (P_f) of the melt in the MDN can be calculated as Eq. (12), where P_{in} is the total pressure at nozzle inlet, and P_{out} is the total pressure at nozzle outlet.

$$P_f = \Delta P = P_{in} - P_{out} \quad (12)$$

In addition, Eq. (13), also called Darcy–Weisbach equation [30], can be used to calculate the pressure drop, where f_D is the flow coefficient, L is the MDN length, and D is the inner-diameter of MDN.

$$P_f = f_D \frac{L}{D} \frac{\rho v^2}{2} \quad (13)$$

Under the assumption that the inner wall of the nozzle is hydraulically smooth, the flow coefficient can be calculated by Blasius equation [31] and Colebrook equation [32] as Eqs. (14) and (15), respectively, where Re is the non-dimensional Reynolds number.

$$f_D = \frac{0.3164}{Re^{0.25}} \quad (14)$$

$$\frac{1}{\sqrt{f_D}} = 1.81 \lg \left(\frac{Re}{6.9} \right) \quad (15)$$

$$Re = \frac{\rho v D}{\mu} \quad (16)$$

3 Results and discussion

3.1 Mesh-sensitivity analysis

For the flow of molten metal in the MDN, the computational domain at the nozzle is crucial and the mesh in this region is supposed to be refined. In addition, the computational domain can be drawn only in half, given that the problem is axisymmetric, as shown in Fig. 1. The middle of the computational domain is the MDN part (DEJK). At zero time, the area on the top is filled with the metal melt (red), and the rest is the air (blue), as shown in Fig. 2.

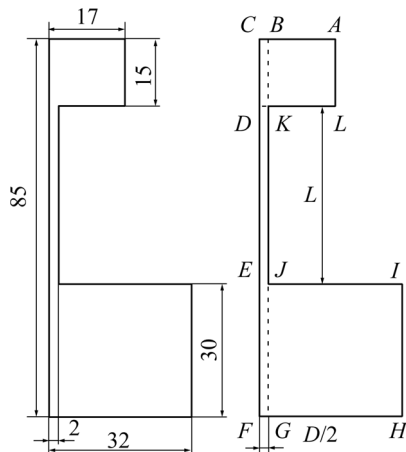


Fig. 1 Computational domain (Unit: mm)

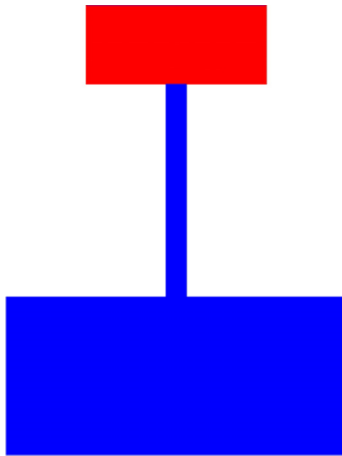


Fig. 2 Physical model (red: liquid metal; blue: air)

Over time, the metal melt gradually flows out of the nozzle under parameter control.

Mesh sensitivity testing was performed by controlling the number of cells across the whole computational domain. The increase in the mesh density is mainly realized through the mesh refinement in the MDN part. Five different numbers of cells are adopted to test the mesh dependence as shown in Table 1. The test and simulation were conducted by ANSYS FLUENT software. In view of the difference in the number of cells, adaptive time step control was applied to keeping the Courant number ($u\Delta t/\Delta x$) less than 0.2, thus maintaining computational stability and accuracy.

Liquid aluminum was selected as testing material, of which the physical parameters are listed in Table 2. In this work, the molten metal is assumed to be fully liquid and has a superheat of 150 K. Under this superheat temperature, the physical parameters of the molten metal, such as viscosity and density, have been corrected based on

Ref. [33]. The pressure inlet and other boundary conditions were set to allow the melt to flow out of the nozzle, as shown in Table 3.

The values of axial velocity on the *DE* axis (see Fig. 1) were extracted for the comparison of simulation results based on different cell numbers, as shown in Fig. 3. When the cell number is larger than 83×10^3 , the distribution curves of axial

Table 1 Meshing control

<i>KJ</i> node number	Number of cells
201	7×10^3
401	29×10^3
601	83×10^3
801	114×10^3
1001	179×10^3

Table 2 Physical properties of molten metals (superheat 150 K) [33]

Material	Density, $\rho/(\text{kg}\cdot\text{m}^{-3})$	Viscosity, $\mu/(\text{mPa}\cdot\text{s})$
Aluminum	2325	1
Iron	6896	4.5
Air	1.225	0.017894
Water	998.2	1.003

Table 3 Boundary conditions

Line segment	Type	Condition
<i>AC</i>	Pressure inlet	3 kPa (Relative atmospheric pressure)
<i>JI, IH, HF</i>	Pressure outlet	Atmosphere
<i>CF</i>	Axis	Symmetry
<i>AL, LK, KJ</i>	Wall	No-slip

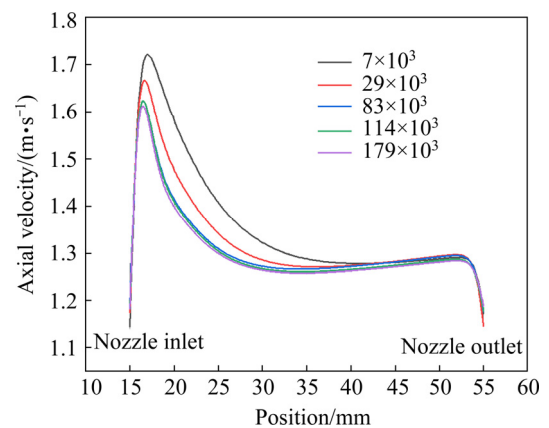


Fig. 3 Distribution curves of axial velocity along center-axis of melt delivery nozzle based on different mesh densities

velocity based on different mesh densities almost coincide with each other. When the number of cells is less than 83×10^3 , the distribution curves of axial velocity based on different mesh densities deviate from each other obviously. Therefore, the mesh consisting of 114×10^3 cells was adopted for the simulation in the present work, achieving a good compromise between computational cost and accuracy.

3.2 Experimental validation

A simulation validation device, of which the main body was a pressure tank, underwent assembly. As shown in Fig. 4(a), the gas cylinder was employed to pressurize the tank to reach the pressure inlet condition in the numerical simulation. Water was selected as the reference material (its physical properties are shown in Table 2). The computational domain was expanded to the same size as the validation device (see Fig. 4(b)). The pressure above the fluid (water) was set to be 5 kPa and the liquid level was 20 mm. Under the above conditions, the total time for water to flow out of the device (flow end time) was obtained from the experiment to validate that from numerical simulation. As shown in Fig. 5, under different MDN inner-diameters, the experimental results of the flow end time of water are basically consistent with those obtained from the numerical simulation. This shows that the numerical simulation method adopted in this work is suitable and reliable for dealing with the problem of liquid flowing in the MDN. On the other hand, the experimental value is higher than that extracted from the numerical simulation, especially when the MDN inner-

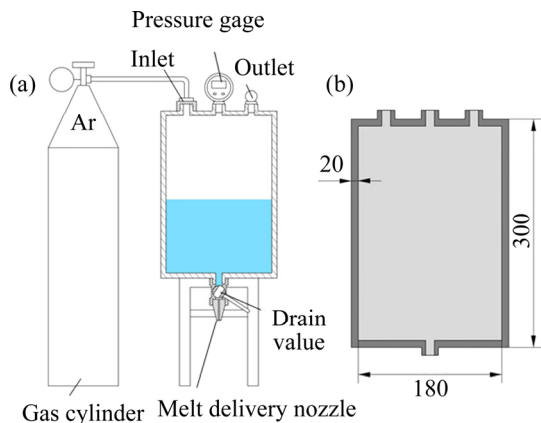


Fig. 4 Schematic diagram (a) and dimensions (b) of validation device (Unit: mm)

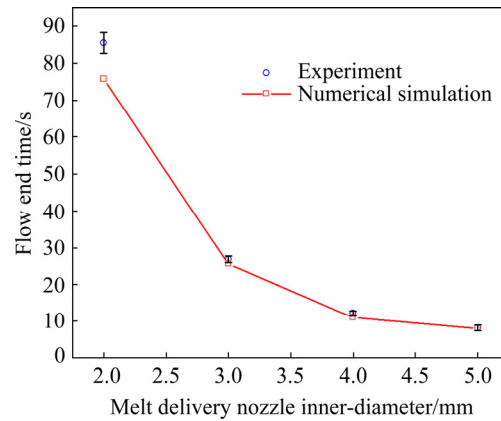


Fig. 5 Comparison of water flow end time through melt delivery nozzles of different inner diameters between validation device experiment and numerical simulation

diameter is 2 mm. The roughness of the valve and the inner wall of the MDN may lead to the increase of the flow time in the experiment, causing the above deviation.

3.3 Flow resistance

For numerical simulation of the melt flow resistance in the nozzle, the MDN part was retained as computational domain to reduce computational cost and facilitate the rapid extraction of resistance data. In addition, the SA turbulence model and low Reynolds number option for SST $k-\omega$ model were introduced for comparison with the SST $k-\omega$ model. The melt mean velocity and the MDN inner-diameter are the two main factors which affect the flow resistance. Therefore, the pressure inlet was changed into the velocity inlet and the effect of surface tension was ignored. The values of total pressure at the inlet and outlet were collected from numerical simulation to calculate the pressure drop caused by the viscous force according to Eq. (12). The numerical results were compared with those from Blasius [31] and Colebrook [32] equations. The liquid aluminum and iron were selected as modeling materials, and the relevant physical properties of these materials are listed in Table 2.

3.3.1 MDN inner-diameter vs flow resistance

The melt velocity in the MDN is in the order of 10^0 – 10^1 m/s during the actual atomization process. The nozzle length of the MDN and the melt velocity were controlled as constants. The MDNs with six different inner-diameters were tested to evaluate the melt flow resistance in the

MDN. As shown in Fig. 6, for molten aluminum, when the nozzle diameter is less than 1 mm, the pressure drop or the flow resistance soars. Under this situation, the melt flow resistance is large, and clogging is likely to occur. As shown in Fig. 7, for molten iron, the relationship between the pressure drop and the nozzle diameter is similar to that of the molten aluminum. As the diameter of the nozzle decreases, the pressure drop increases. In general, the pressure drop of molten iron is larger than that of molten aluminum, which is about three times the latter, indicating that the molten iron is more resistant to flow than the molten aluminum in the MDN. On the other hand, the results based on the SA, SST $k-\omega$, and SST $k-\omega$ -LRe turbulence models exhibit the similar variation trends, with no significant difference. The numerical results of the pressure drop obtained based on the turbulence models above agree with those calculated by Blasius [31] and Colebrook [32] equations

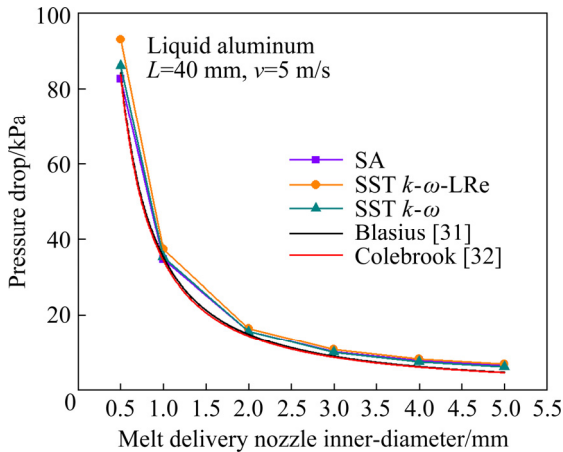


Fig. 6 Relationship between pressure drop of molten aluminum and inner-diameter of melt delivery nozzle

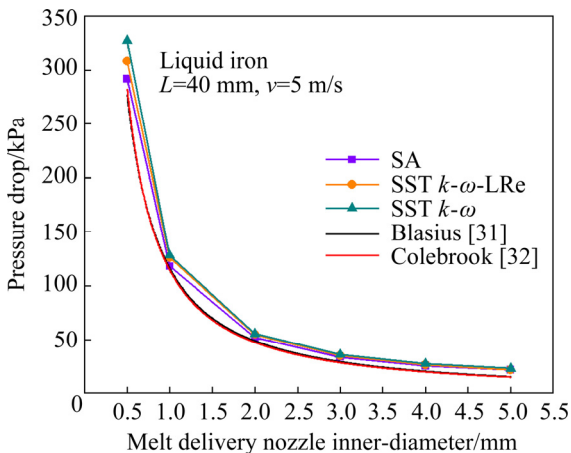


Fig. 7 Relationship between pressure drop of molten iron and inner-diameter of melt delivery nozzle

reasonably, but the numerical results are relatively high, especially in the case of nozzle diameter less than 1 mm. This may be attributed to the fact that the calculations based on Blasius [31] and Colebrook [32] equations assume a fully developed turbulent flow. Additionally, when the SST $k-\omega$ turbulence model is coupled with low Reynolds number correction (SST $k-\omega$ -LRe), the numerical results for the pressure drop of molten iron are closer to those calculated by the empirical formulas, while numerical results of the pressure drop of molten aluminum show greater deviation. This difference is due to the different Reynolds numbers of the two melt flows. When the MDN inner-diameter changes from 0.5 to 5 mm, the range of Reynolds number of molten iron is $(3.8-38)\times 10^3$, while that of molten aluminum is $(5.8-58)\times 10^3$. Therefore, low Reynolds number correction is more effective for the pressure drop calculation in a low Reynolds number range.

3.3.2 Mean velocity vs flow resistance

Further, for the fixed length and inner-diameter of the melt nozzle, the melt mean velocity in the MDN was changed to study the effect of the melt mean velocity on the pressure drop. The SST $k-\omega$ turbulence model was adopted and the molten aluminum was chosen as modeling material. As shown in Fig. 8, as the melt mean velocity increases, the pressure drop also increases, but there is no sudden increase in pressure drop in the specific velocity range. The numerical simulation results indicate similar variation trend with those calculated from Blasius [31] and Colebrook [32] equations, but the values of the former are higher.

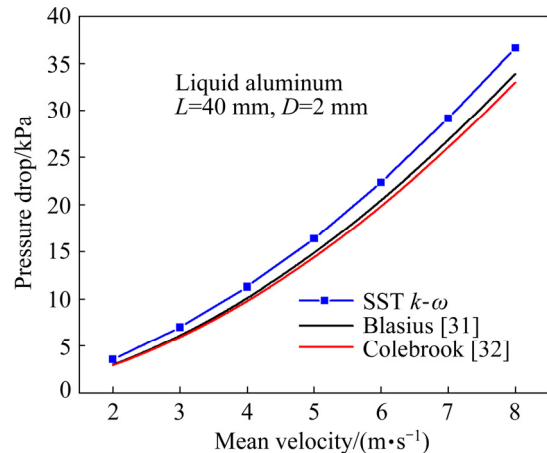


Fig. 8 Relationship between pressure drop of molten aluminum and mean velocity

3.3.3 Summary

The simulation results show that the increase of melt mean velocity and the decrease of MDN diameter can cause the increase of flow resistance. The flow resistance is essentially expressed by the shear stress (τ), as the force per unit area requires to move a fluid layer. The shear stress depends on how much the fluid layers are displaced against each other. This in turn is expressed by the velocity gradient perpendicular to the flow direction, which is the slope of the velocity profile in the radial direction. The mathematical relationship between these two quantities is described as

$$\tau = \mu \frac{dv(r)}{dr} \quad (17)$$

where $v(r)$ is the velocity profile in the radial direction, and r is the radial distance. Here, the melt flow in the MDN is assumed to be Newtonian fluid. As shown in Fig. 9, the melt velocity is the maximum at the centreline of the MDN and is zero on the wall (no-slip condition). When the MDN inner-diameter is fixed, the maximum velocity increases as the melt mean velocity increases. In this case, the velocity gradient increases from the centreline to the wall (radial direction), which leads to an increase in flow resistance. On the other hand, when the melt velocity is fixed, as the MDN inner-diameter decreases, the melt velocity is reduced from the maximum to zero in a shorter distance from the centreline to the wall. This means that the velocity gradient in the radial direction also increases with the decrease of the MDN inner-diameter, which increases the melt flow resistance.

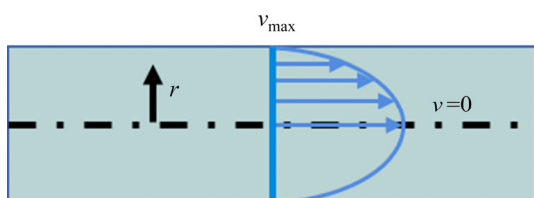


Fig. 9 Velocity profile in radial direction in melt delivery nozzle (MDN)

The effects of the MDN diameter and the melt mean velocity on the pressure drop are compared in Fig. 10. It can be found that the changing rate of the pressure drop based on the MDN diameter is larger than the melt mean velocity. This means that the MDN diameter has a greater effect on the melt flow

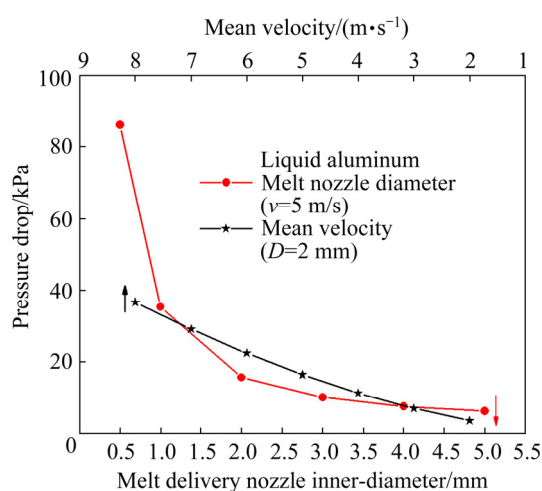


Fig. 10 Comparison of influence of melt delivery nozzle inner-diameter and melt mean velocity on pressure drop

resistance in the MDN than the melt mean velocity within the parameters studied.

3.4 High viscosity aluminum alloy powder production

3.4.1 Experimental setup

A self-designed high-temperature aluminum alloy was atomized, and its chemical composition is shown in Table 4. Due to the addition of a large amount of silicon (Si) and iron (Fe), the viscosity of the molten alloy increased significantly. Therefore, it is difficult for the molten alloy to flow out of the MDN only driven by its own gravity and the aspiration pressure in front of the MDN exit during the GA process. In a conventional GA process, the MDN with a large inner-diameter (> 4 mm) must be employed for the atomization of such viscous melts in case that the MDN is clogged. However, this will result in very low yield of fine powders. In the present work, the positive pressure (P_+) is imposed on the melt, as an additional driving force, to push the melt to flow out of the MDN. The way that imposes positive pressure on the molten metal is similar to that in the verification device (Fig. 4). As shown in Fig. 10, the alloy melt flows out of the MDN under the positive pressure and is subsequently atomized by the atomizing gas. The atomizer is a discrete jet nozzle with 20 straight bore holes ($\Phi 0.8$ mm \times 20) in a quasi-close-coupled configuration. The material of the MDN is graphite. Three different MDN inner-diameters are tested, i.e., 4, 3 and 2 mm. Given the alloy melt is more viscous than the pure metal melt, the positive

pressure imposed on the alloy melt is set in a range of 30–40 kPa, higher than those calculated values of the pressure drop of the aluminum melt in the MDN (see Fig. 6). In the experiments, the value of the positive pressure imposed on the melt increases linearly as the MDN inner-diameter decreases. The atomizing gas is pure nitrogen and the atomization pressure is maintained at 2 MPa. As shown in Fig. 11, the atomization angle is defined as an angle between two opposite gas jets, which is designed as 40° in this study. Atomization parameters are listed in Table 5.

Table 4 Chemical composition of self-designed aluminum alloy (wt.%)

Si	Fe	Mg	Cu	Al
18–20	5.0–6.0	1.0–1.6	3.2–4.4	Bal.

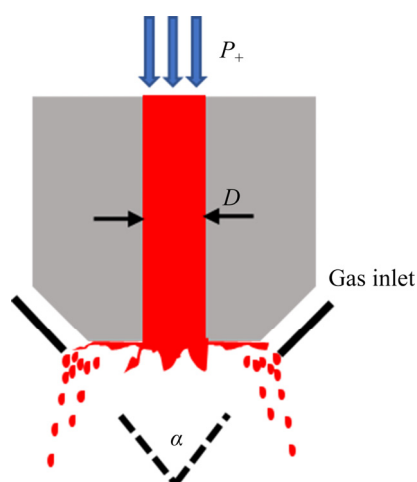


Fig. 11 Schematic diagram of gas atomization process by introducing positive pressure on melt through melt delivery nozzle

3.4.2 Powder characterization

Particle size distributions were obtained with a Bechman-Coulter LS13 320 particle size analyzer. The yield of powder below 150 μm was extracted from laser diffraction and sieve analysis. Powder morphology was observed by scanning electron microscopy (SEM) (JEOL JSM–6510).

As shown in Fig. 12, when the MDN inner-diameter decreases, the cumulative volume distribution curve of particle size becomes steeper. This indicates that the particle size of powders becomes smaller with the decrease of the MDN inner-diameter. It becomes obvious that the fine powder yield ($<150 \mu\text{m}$) declines with the increase of the MDN inner-diameter, as shown in Fig. 13. Due to the different test methods, the powder yield results show a certain deviation. However, compared with the MDN inner-diameter ($D=4 \text{ mm}$), the fine powder yield is significantly improved when $D=2 \text{ mm}$, from 59.6% to 94.4% (laser diffraction), and from 54.7% to 94.2% (sieve analysis), respectively.

Figure 14 presents a view of the powders at the same magnification which were produced under different MDN inner-diameters. Obviously, all the prepared powders are basically spherical or nearly spherical. The shrinkage of the MDN inner-diameter leads to an increase in the quantity of fine powders, which is consistent with the particle size analysis results. When the diameter of the MDN is greater than 2 mm, the number of satellite particles, i.e., those small particles sticking on the surface of large particles, gradually increases. Figure 15 presents a partial enlarged view of satellite particles. It can be found that the adhesion of small particles on the surface of large particles is more obvious. The solidification time of the droplet becomes longer as the droplet size increases. When small droplets solidify into particles, large droplets remain molten. In this case, satellite particles are formed when they collide with each other [34].

The specific particle sizes have been determined, including D_{90} , D_{50} , and D_{10} (the corresponding particle size when the cumulative volume fraction of powders achieves 90%, 50%, and 10%, respectively). As shown in Fig. 16, D_{50} , also known as the median diameter, is positively related to the MDN inner-diameter. Thus, using the MDN with a smaller inner-diameter can effectively

Table 5 Atomization parameters

MDN diameter/mm	Positive pressure/kPa	Gas pressure/MPa	Gas mass flow rate/($\text{kg}\cdot\text{min}^{-1}$)	Melt mass flow rate/($\text{kg}\cdot\text{min}^{-1}$)	GMR	Melt velocity/($\text{m}\cdot\text{s}^{-1}$)
4	30	2	3.3	3.4	1.0	1.9
3	35	2	3.3	3.1	1.1	3.0
2	40	2	3.3	1.7	1.9	3.8

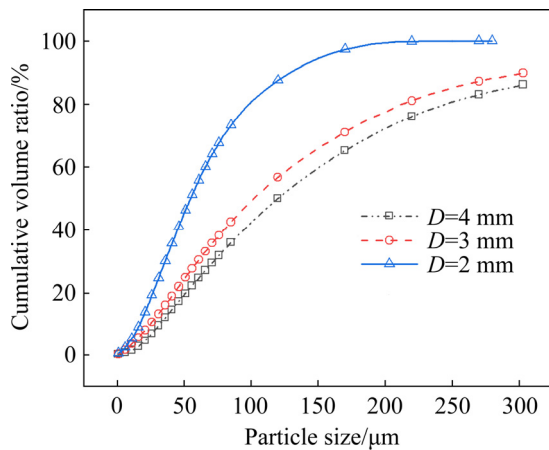


Fig. 12 Particle size distribution of gas-atomized powders prepared by use of melt delivery nozzles with different inner-diameters (D)

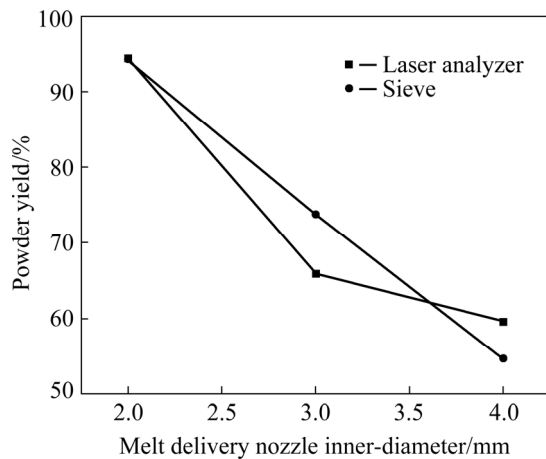


Fig. 13 Relationship between fine powder yield (<150 μm) and melt delivery nozzle inner-diameter

reduce the median diameter. In addition, with the increase of the MDN inner-diameter, the deviation between D_{90} and D_{10} becomes larger, which implies that the collision frequency between small particles and large droplets will rise during GA process.

According to the Lubanska correlation [35], the relationship between the median diameter (D_{50}) and atomization parameters can be described by

$$D_{50} = K \frac{1}{V_{GM}} \left[D \left(1 + \frac{1}{R} \right) \right]^{\frac{1}{2}} \quad (18)$$

where K is a constant, V_{GM} is the relative velocity between gas and melt, and GMR (R) is the gas to melt mass flow rate. In the atomization experiments, the melt velocity is within the range of 1–5 m/s. Relative to the atomization gas velocity (about 200–300 m/s), the variation of melt velocity can be negligible. Therefore, the relative velocity (V_{GM})

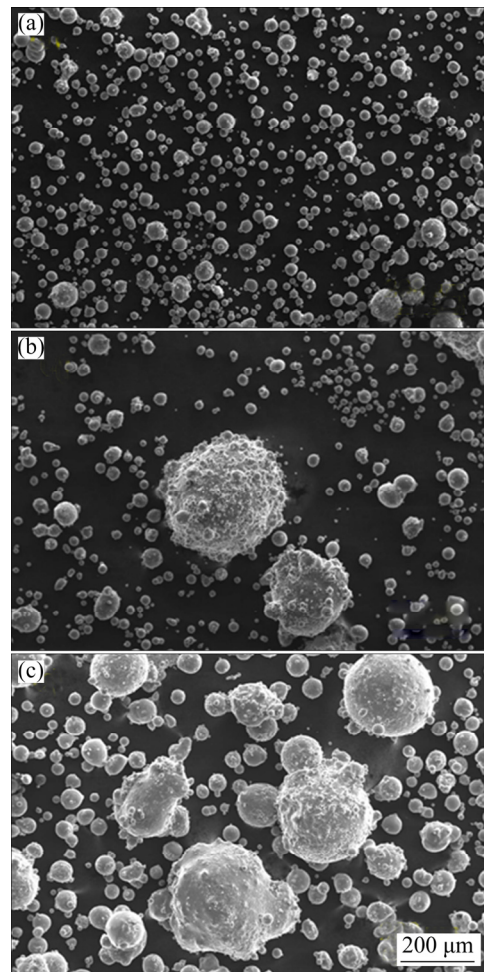


Fig. 14 SEM images of powders with different MDN inner-diameters: (a) $D=2$ mm; (b) $D=3$ mm; (c) $D=4$ mm

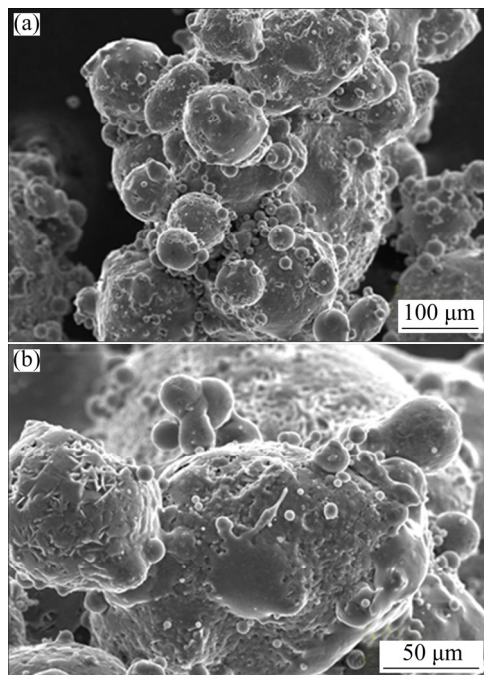


Fig. 15 SEM images of satellite particles ($D=4$ mm) with different magnifications

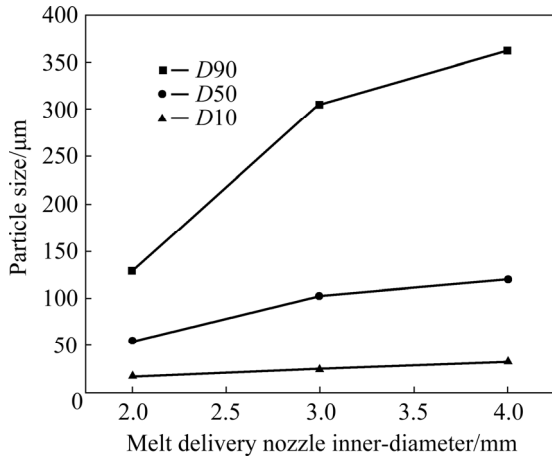


Fig. 16 Relationship between specific particle size and melt delivery nozzle inner-diameter

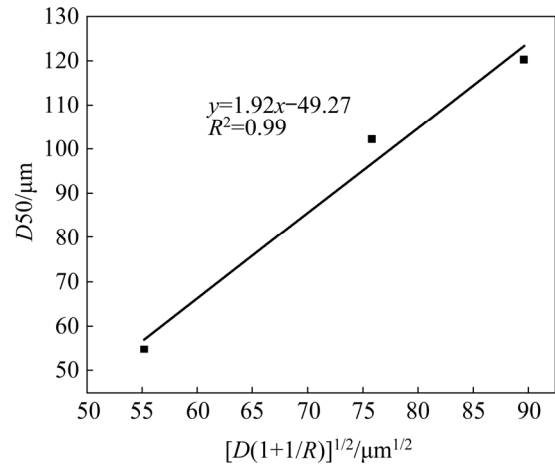


Fig. 17 Relationship between $D50$ and $[D(1+1/R)]^{0.5}$

can be regarded as a constant at a fixed atomization pressure. This means that the median diameter ($D50$) is only related to the two parameters, i.e., gas to melt mass flow rate ratio (GMR) and MDN inner-diameter (D). As shown in Fig. 17, the variation of $D50$ with $[D(1+1/R)]^{0.5}$ is basically linear, which is consistent with Eq. (18). When other parameters are fixed, an increase in melt velocity will reduce GMR, which leads to an increase in $D50$, ultimately reducing the yield of fine powder. The melt velocity is mainly controlled by the MDN inner-diameter and the positive pressure imposed on the melt. A smaller MDN inner-diameter reduces the melt velocity, while a positive pressure enhances the melt velocity. After imposing the positive pressure, the molten metal can flow out from a smaller inner-diameter MDN. It can be found from Eq. (18) that the median diameter is proportional to the square root of the MDN inner-diameter. This means that the reduction in the MDN inner-diameter itself will also lead to a reduction in the median diameter. As shown in Table 5, the melt mass flow rate decreases as the MDN inner-diameter decreases, in spite of the increase in the melt velocity. In this case, the fine powder yield can be significantly improved because of the combined effects of the reduction in MDN inner-diameter and the increase of GMR.

The standard deviation is often employed to reflect the degree of dispersion of a set of data. In this work, the arithmetic standard deviation (defined as Eq. (19)) of powder particle size is introduced to characterize the unevenness of powder particle size distribution:

$$\sigma = \sqrt{\frac{\sum_{i=1}^n (d_i - \bar{d})^2}{n}} \tag{19}$$

where σ is the standard deviation, n is the number of particle swarm, d_i represents the particle size of arbitrary particle, and \bar{d} is the average particle size. A higher dispersion degree of particle size indicates a larger deviation in droplet motion state and solidification time during GA process. In this case, the particle/droplet collision frequency will increase, thus enhancing the sticking of small particles on large droplets. That is, the larger the standard deviation, the larger the number of satellite particles. As shown in Fig. 18, compared with $D=2$ mm, when the MDN diameter is 3 or 4 mm, the standard deviation value is much larger. This indicates that when $D=3$ mm or 4 mm, the satellite particle phenomenon is much more obvious in the

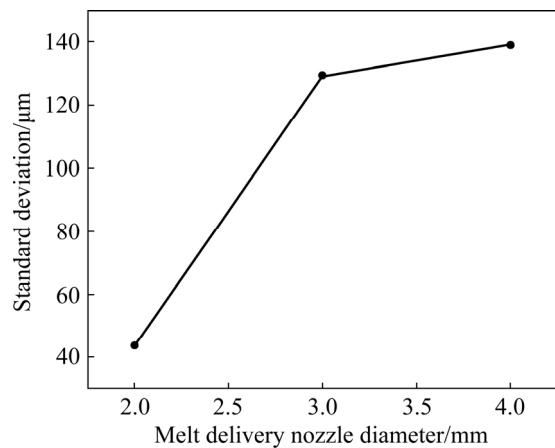


Fig. 18 Relationship between particle size standard deviation and melt delivery nozzle inner-diameter

prepared powder than that under $D=2$ mm. Overall, employing a small inner-diameter MDN is not only beneficial to raising the fine powder yield, but also helps to reduce the quantity of satellite particles. However, in this case, an additional driving force is needed to counterbalance the large melt flow resistance in the MDN with a small inner-diameter, e.g., the positive pressure imposed on the melt here.

4 Conclusions

(1) The numerical simulation is proved to be an effective and low-cost tool for predicting the melt flow process in the MDN. By ignoring the roughness of the MDN inner-wall, the numerical models predicted slightly lower values of flow end time of liquid through the MDN than those from the experiments, especially the deviation being larger in the case of a small MDN inner-diameter. The numerical models generally predicted higher values of melt pressure drop than those empirical correlations based on a fully developed liquid flow, especially in the case of the MDN with a diameter less than 1 mm.

(2) The numerical calculation results indicate that the melt pressure drop in the MDN increases quickly with the decrease of the MDN inner-diameter, and varies in an order of 10^0 – 10^2 kPa for both aluminum and iron melts when the MDN inner-diameter reduces from 5.0 to 0.5 mm. Moreover, the melt pressure drop in the MDN and the mean velocity are positively correlated.

(3) The positive pressure (30–40 kPa) was imposed on the melt against the melt flow resistance in MDNs with different inner-diameters (from 4 to 2 mm), ensuring a smooth melt flow. Compared with the traditional GA process, this method can produce higher viscosity alloy powder with a smaller MDN diameter. The MDN with a small inner-diameter can enhance the fine powder yield and improve the powder surface quality.

Acknowledgments

The authors are grateful for the financial supports from the National Natural Science Foundation of China (No. 52074157), Shenzhen Science and Technology Innovation Commission, China (Nos. JSGG20180508152608855, KQTD20170328154443162), and Shenzhen Key Laboratory for Additive Manufacturing of

High-performance Materials, China (No. ZDSYS201703031748354).

References

- [1] ANDERSON I E, WHITE E M H, DEHOFF R. Feedstock powder processing research needs for additive manufacturing development [J]. *Current Opinion in Solid State and Materials Science*, 2018, 22(1): 8–15. DOI: 10.1016/j.cossms.2018.01.002
- [2] XU De, GAO Hua-bing, DONG Tao, CUI Chuan-yu, YANG Zhen-lin, LI Hai-xin, JIANG Feng-chun, WANG Jian-dong. Research progress of metal powder for additive manufacturing [J]. *The Chinese Journal of Nonferrous Metals*, 2021, 31(2): 245–257. DOI: 10.11817/j.ysxb.1004.0609.2021-37728. (in Chinese)
- [3] LI Xing-gang, LIU Chang, ZHU Qiang. Research progress on gas atomization technology for preparation of feedstock powder used in metal additive manufacturing [J]. *Aeronautical Manufacturing Technology*, 2019, 62(22): 22–34. DOI: 10.16080/j.issn1671-833x.2019.22.022. (in Chinese)
- [4] DAWES J, BOWERMAN R, TREPLETEON R. Introduction to the additive manufacturing powder metallurgy supply chain [J]. *Johnson Matthey Technology Review*, 2015, 59(3): 243–256. DOI: 10.1595/205651315X688686.
- [5] LEFEBVRE A H, MCDONELL V G. *Atomization and sprays* [M]. 2nd ed. Boca Raton: CRC Press, 2017. DOI: 10.1201/9781315120911.
- [6] LI Xin-wei, SHI Shi, HAN Shuang, HU Xiao-gang, ZHU Qiang, LU Hong-xing, LI Wen-wu, DING Hui, SHI Yu-sheng. Microstructure, solidification behavior and mechanical properties of Al–Si–Mg–Ti/TiC fabricated by selective laser melting [J]. *Additive Manufacturing*, 2020, 34: 101326. DOI: 10.1016/j.addma.2020.101326.
- [7] GAO Cao-feng, XIAO Zhi-yu, ZOU Hai-ping, LIU Zhong-qiang, CHEN Jin, LI Shang-kui, ZHANG Da-tong. Characterization of spherical AlSi10Mg powder produced by double-nozzle gas atomization using different parameters [J]. *Transactions of Nonferrous Metals Society of China*, 2019, 29(2): 374–384. DOI: 10.1016/S1003-6326(19)64947-2.
- [8] CAI Zhi-yong, ZHANG Chu, WANG Ri-chu, PENG Chao-qun, WU Xiang, LI Hai-pu, YANG Ming. Improvement of deformation capacity of gas-atomized hypereutectic Al–Si alloy powder by annealing treatment [J]. *Transactions of Nonferrous Metals Society of China*, 2018, 28(8): 1475–1483. DOI: 10.1016/S1003-6326(18)64795-8.
- [9] ZHAO Shao-yang, CHEN Gang, TAN Pin, WANG Jian, LIU Xiao-qing. Characterization of spherical TC4 powders by gas atomization and its interstitial elemental control [J]. *The Chinese Journal of Nonferrous Metals*, 2016, 26(5): 980–987. DOI: 10.19476/j.ysxb.1004.0609.2016.05.005. (in Chinese)
- [10] CACACE S, SEMERARO Q. Influence of the atomization medium on the properties of stainless steel SLM parts [J].

- Additive Manufacturing, 2020, 36: 101509. DOI: 10.1016/j.addma.2020.101509.
- [11] LI Gan, GUO Cheng, GUO Wen-feng, LU Hong-xing, WEN Lin-ju, HU Xiao-gang, ZHU Qiang. Influence of selective laser melting process parameters on densification behavior, surface quality and hardness of 18Ni300 steel [J]. Key Engineering Materials, 2020, 861: 77–82. DOI: 10.4028/www.scientific.net/KEM.861.77.
- [12] ZHOU Shang-chen, ZHANG Peng, XUE Yun-fei, WANG Fu-chi, WANG Lu, CAO Tang-qing, TAN Zhen, CHENG Bao-yuan, WANG Ben-peng. Microstructure evolution of Al_{0.6}CoCrFeNi high entropy alloy powder prepared by high pressure gas atomization [J]. Transactions of Nonferrous Metals Society of China, 2018, 28(5): 939–945. DOI: 10.1016/S1003-6326(18)64728-4.
- [13] LEHTONEN J, GE Yan-ling, CIFTCI N, HECZKO O, UHLENWINKEL V, HANNULA S P. Phase structures of gas atomized equiatomic CrFeNiMn high entropy alloy powder [J]. Journal of Alloys and Compounds, 2020, 827: 154142. DOI: 10.1016/j.jallcom.2020.154142.
- [14] HENEIN H, UHLENWINKEL V, FRITSCHING U. Metal sprays and spray deposition [M]. Cham: Springer, 2017: 89–176. DOI: 10.1007/978-3-319-52689-8_4.
- [15] TONG Ming-ming, BROWNE D J. Modelling compressible gas flow near the nozzle of a gas atomiser using a new unified model [J]. Computers & Fluids, 2009, 38(6): 1183–1190. DOI: 10.1016/j.compfluid.2008.11.014.
- [16] MOTAMAN S, MULLIS A M, COCHRANE R F, MCCARTHY I N, BORMAN D J. Numerical and experimental modelling of back stream flow during close-coupled gas atomization [J]. Computers & Fluids, 2013, 88: 1–10. DOI: 10.1016/j.compfluid.2013.08.006.
- [17] ZEOLI N, TABBARA H, GU S. CFD modeling of primary breakup during metal powder atomization [J]. Chemical Engineering Science, 2011, 66(24): 6498–6504. DOI: 10.1016/j.ces.2011.09.014.
- [18] LI Xing-gang, FRITSCHING U. Process modeling pressure-swirl-gas-atomization for metal powder production [J]. Journal of Materials Processing Technology, 2017, 239: 1–17. DOI: 10.1016/j.jmatprotec.2016.08.009.
- [19] LAMPA A, FRITSCHING U. Large eddy simulation of the spray formation in confinements [J]. International Journal of Heat and Fluid Flow, 2013, 43: 26–34. DOI: 10.1016/j.ijheatfluidflow.2013.04.014.
- [20] MULLIS A M, MCCARTHY I N, COCHRANE R F. High speed imaging of the flow during close-coupled gas atomisation: Effect of melt delivery nozzle geometry [J]. Journal of Materials Processing Technology, 2011, 211(9): 1471–1477. DOI: 10.1016/j.jmatprotec.2011.03.020.
- [21] SCHWENCK D, ELLENDT N, FISCHER-BÜHNER J, HOFMANN P, UHLENWINKEL V. A novel convergent-divergent annular nozzle design for close-coupled atomization [J]. Powder Metallurgy, 2017, 60(3): 198–207. DOI: 10.1080/00325899.2017.1291098.
- [22] SHU Shi, LI Xing-gang, LIU Xi-kui, FAN Jian-zhong, ZHANG Shao-ming. Coupled pressure-gas atomization process for fine spherical aluminium alloy powder production [J]. Chinese Journal of Rare Metal, 2018, 43(8): 808–815. DOI: 10.13373/j.cnki.cjrm.xy18010030. (in Chinese)
- [23] LI Xing-gang, ZHU Qiang, SHU Shi, FAN Jian-zhong, ZHANG Shao-ming. Fine spherical powder production during gas atomization of pressurized melts through melt nozzles with a small inner diameter [J]. Powder Technology, 2019, 356: 759–768. DOI: 10.1016/j.powtec.2019.09.023.
- [24] COTTON W R, BRYAN G, van den HEEVER S C. Storm and cloud dynamics: The dynamics of clouds and precipitating mesoscale systems [M]. 2nd ed. Burlington, San Diego, London: Academic Press, 2011: 53–86. DOI: 10.1016/S0074-6142(10)09909-2.
- [25] SPALART P, ALLMARAS S. A one-equation turbulence model for aerodynamic flows [C]//30th Aerospace Sciences Meeting and Exhibit. Reno, NV: AIAA, 1992: 439. DOI: 10.2514/6.1992-439.
- [26] WILCOX D C. Turbulence modeling for CFD [M]. Glendale, CA: DCW Industries Inc., 1993.
- [27] LAUNDER B E, SPALDING D B. Mathematical models of turbulence [M]. New York: Academic Press, 1972.
- [28] MENTER F R. Two-equation eddy-viscosity turbulence models for engineering applications [J]. AIAA Journal, 1994, 32(8): 1598–1605. DOI: 10.2514/3.12149.
- [29] ANDERSON J D. Fundamentals of aerodynamics [M]. 5th ed. New York: McGraw-Hill Education, 2010.
- [30] BROWN G O. The history of the Darcy-Weisbach equation for pipe flow resistance [C]//Environmental and Water Resources History at ASCE Civil Engineering Conference and Exposition 2002. Washington DC: ASCEM, 2002: 34–43.
- [31] BLASIUS H. The law of similarity in friction process in liquids [M]. Berlin, Heidelberg: Springer, 1913: 1–41. (in German)
- [32] COLEBROOK C F. Turbulent flow in pipes with particular reference to the transition region between the smooth and rough pipe laws [J]. Journal of the Institution of Civil Engineers, 1939, 11: 133–156.
- [33] ASSAEL M J, KAKOSIMOS K, BANISH R M, BRILLO J, EGRY I, BROOKS R, QUESTED P N, MILLS K C, NAGASHIMA A, SATO Y, WAKEHAM W A. Reference data for the density and viscosity of liquid aluminum and liquid iron [J]. Journal of Physical and Chemical Reference Data, 2006, 35(1): 285–300. DOI: 10.1063/1.2149380.
- [34] ÖZBILEN S. Satellite formation mechanism in gas atomised powders [J]. Powder Metallurgy, 1999, 42(1): 70–78. DOI: 10.1179/pom.1999.42.1.70.
- [35] LUBANSKA H. Correlation of spray ring data for gas atomization of liquid metals [J]. JOM, 1970, 22: 45–49. DOI: 10.1007/BF03355938.

气体雾化制粉工艺中金属熔体在导流管内流动过程的数值研究

刘畅^{1,2}, 李欣^{1,2}, 舒适³, 黄禹赫^{1,4}, 黎兴刚^{1,2,4}, 朱强^{1,2}

1. 南方科技大学 机械与能源工程系, 深圳 518055;
2. 深圳市高机能材料增材制造重点实验室, 深圳 518055;
3. 湖南兵器技术中心有限公司, 长沙 410201;
4. 南方科技大学 前沿与交叉科学研究院, 深圳 518055

摘要: 基于流体体积(VoF) 界面捕捉方法和剪切应力输运(SST $k-\omega$) 湍流模型, 通过数值模拟揭示气体雾化制粉工艺中金属熔体在导流管内的流动机理。验证实验表明, 数值模型能对导流管内的流体流动过程进行合理预测。随着导流管内径的减小, 熔融铝和熔融铁的流动阻力增大, 当导流管内径减小至 1 mm 时, 熔体的流动阻力可达 10^2 kPa 数量级。基于传统的气体雾化工艺, 在金属熔体上方施加正向压力克服熔体在导流管内的流动阻力并在不同导流管内径下雾化高黏性铝合金熔体。当导流管内径从 4 mm 减小到 2 mm 时, 粉末的细粉收得率 ($<150 \mu\text{m}$) 从 54.7% 大幅增加到 94.2%。当采用较小内径的导流管时, 粉末的表面质量也有所改善。

关键词: 气体雾化; 导流管; 熔融金属; 流体阻力; 金属粉末

(Edited by Xiang-qun LI)